Coupled crystal and magnetic chiralities in $NiCo_2TeO_6$ determined by polarized x-ray and neutron scattering

N. Qureshi [1,*] A. M. Vibhakar [2] K. Beauvois [3] J. A. Rodríguez-Velamazán [1] A. Stunault,[1] R. Scatena [2] F. Carneiro [2] A. Bombardi [2] C. J. Won [4] K. Du,[5] and S.-W. Cheong[4,5]

[1]*Institut Laue-Langevin, 71 avenue des Martyrs, CS 20156, 38042 Grenoble Cedex 9, France*

[2]*Diamond Light Source, Chilton, Didcot, Oxfordshire OX11 0QX, United Kingdom*

[3]*Université Grenoble Alpes, CEA, IRIG, MEM, MDN, 38000 Grenoble, France*

[4]*Laboratory for Pohang Emergent Materials and Max Planck POSTECH Center for Complex Phase Materials, Pohang University of Science and Technology, Pohang 37673, South Korea*

[5]*Keck Center for Quantum Magnetism and Department of Physics and Astronomy, Rutgers University, Piscataway, New Jersey 08854, USA*

(Received 2 December 2025; revised 20 January 2026; accepted 10 February 2026; published 6 March 2026)

We present a combined x-ray and polarized neutron scattering study on chiral, polar and magnetoeletric $NiCo_2TeO_6$ single crystals with different net crystal chiralities as characterized by optical methods. The rastering images taken with a micrometer-sized polarized x-ray beam unambiguously reveal the coupling of crystal and magnetic chiralities in a heterochiral sample. Spherical neutron polarimetry experiments on a different, structurally enantiopure sample—as evidenced by polarized x-ray scattering—reveal a homochiral magnetic spiral, which proves the stabilization of a single helical handedness despite the intertwined structural helices in the ferri-chiral crystal structure.

DOI: 10.1103/mxdc-pl82

I. INTRODUCTION

Noncentrosymmetric compounds have attracted growing attention due to their rich array of physical phenomena that emerge from the absence of inversion symmetry. A particularly intriguing consequence is the emergence of structural chirality, where atomic arrangements give rise to handed crystal structures that cannot be superimposed on their mirror images. In recent years, the interplay between chirality and magnetism in such materials has revealed novel magnetic behaviors, including nonreciprocal transport effects [1], and the stabilization of topological spin textures such as skyrmions [2,3]. These effects often stem from the antisymmetric Dzyaloshinskii-Moriya interaction, which becomes active in noncentrosymmetric environments. Understanding how chirality influences magnetic properties is thus essential for advancing the design of functional magnetic materials with applications in spintronics and beyond. Nickelates are noncentrosymmetric compounds that display a variety of interesting physics, ranging from large optical activity to colossal magnetoelectric response, both highly interesting concepts for the realization of functional materials. $Ni_{3-x}M_xTeO_6$ where M = Co or Mn crystallizes in the noncentrosymmetric trigonal space group $R3$. The crystal structure derives from the centrosymmetric corundum (Al_2O_3) structure with space group $R\bar{3}c$, where the introduction of Te and M onto nominally Al sites breaks the inversion and c-glide symmetry present in the parent aristotype structure, giving rise to the formation of six chiral and six polar domains. Triangular plaquettes that form between the oxygen anions on two distinct crystallographically inequivalent sites (labeled O1 and O2) above and below the cations rotate by 120° between each Ni layer. In $R\bar{3}c$ symmetry the O1 and O2 plaquettes are identical owing to the c-glide plane relating them. However, in $R3$ symmetry the c-glide plane is broken and the two plaquettes are no longer identical, which gives rise to a net chiral structure [4]. Ni_3TeO_6 exhibits—in contrast to other compounds with corundum-related structures, such as α-Al_2O_3, Cr_2O_3, or $LiNbO_3$—both chirality and polarity with a large optical specific rotation with application potential. The chiral and polar domains were found to be interlocked with a one-to-one correspondence, such that each chiral domain was also found to be a single polar domain [4], which results from minimized lattice distortions at the domain walls. In a more recent study [5], synchrotron-based near-field infrared nanospectroscopy reveals that charged domain walls are twice as wide as neutral walls due to added strain created at the interface.

In Ni_3TeO_6, the magnetic moments of the Ni^{2+} ions order below $T_N = 53$ K in a commensurate collinear antiferromagnetic structure with ferromagnetic a-b planes of spins aligned along c and stacked antiferromagnetically along c according to a T-point propagation vector $\mathbf{k} = (0\ 0\ \frac{3}{2})$ [7]. Concomitant with the transition to long-range magnetic order is the development of a small electrical polarization that reaches $3280\,\mu Cm^{-2}$ at 2 K [8]. A study of the magnetoelectric coupling by a combination of infrared, Raman and time-domain THz spectroscopic techniques revealed at least two spin excitations in the antiferromagnetic phase that can be assigned to electromagnons [9]. Upon application of a large magnetic field (∼8 T) a spin-flop transition was observed, such that

*Contact author: qureshi@ill.fr

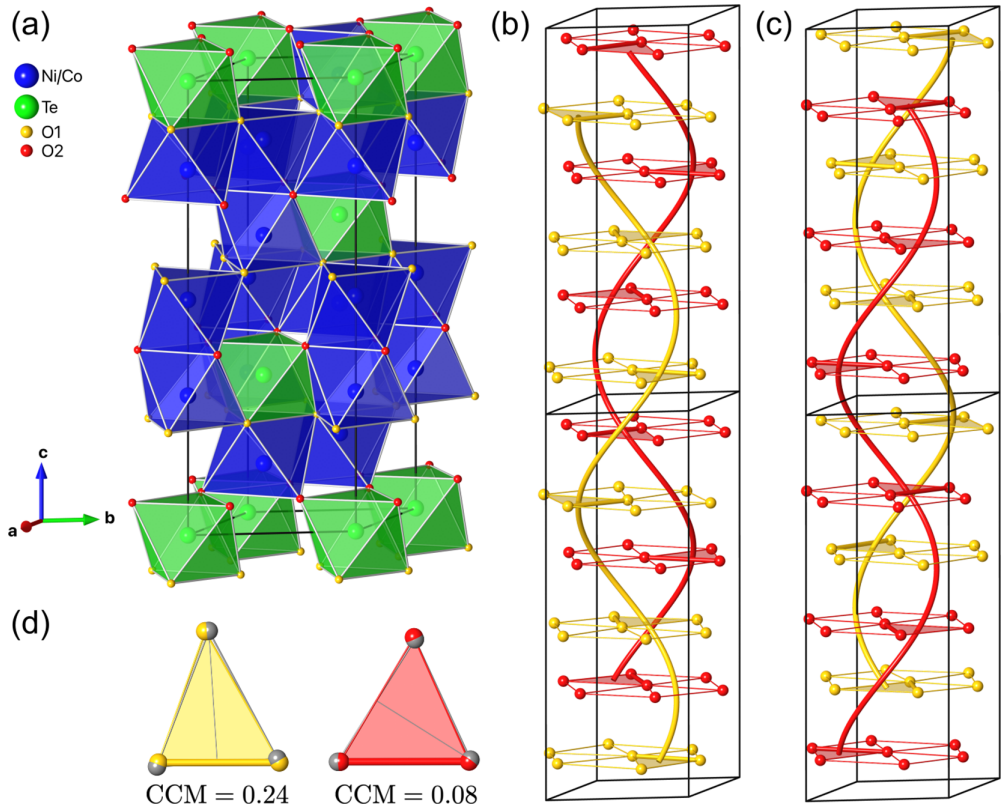

FIG. 1. (a) Crystal structure of $NiCo_2TeO_6$ in the trigonal $R3$ space group (hexagonal setting) emphasizing the complex network of edge- and facesharing MO_6 and TeO_6 octahedra. The atomic positions and lattice parameters have been taken from [6] (low-temperature D2B data). (b) shows O1 and O2 atoms only, while focusing on the chiral aspects of the crystal structure. Highlighted triangles represent triangles with three different bond lengths, from which the shortest O1-O1 or O2-O2 bond is marked by a thicker cylinder. The yellow and red spirals propagating along the c axis reveal the opposite handednesses of the O1 and O2 triangle screw. (c) shows the inversion twin of (b) in which the respective chiralities are inverted. (d) Visualization of the continuous chirality measure concept on the two relevant structural fragments, the O1 (yellow) and O2 (red) triangles as emphasized in (b) and (c). The yellow and red triangles are viewed along the c axis and the gray atoms indicate the positions for an isosceles and therefore achiral triangle. The minimal distance, by which the atoms have to be shifted in the yellow triangle is larger than in the red triangle, for which the continuous chirality measure for the yellow triangles is larger and constitutes the majority chirality in the ferri-chiral structure. Therefore, the structure in (b) reveals an overall right-handed chirality, while (c) is the left-handed counterpart.

the magnetic structure transformed into an incommensurate conical spiral with propagation vector $\mathbf{k} = (0\ 0\ \frac{3}{2} \pm \delta)$ where $\delta \sim 0.18$ [10]. The spin-flop transition proceeds through a narrow intermediate spin state, which is responsible for the magnetoelectric switching to occur without any hysteretic behavior. The resulting colossal magnetoelectric response is highly interesting for the realization of practical magnetoelectric devices with high tunability and good retention [8].

Co substitution in Ni_3TeO_6 preserves the magnetoelectric properties of the parent compound and enhances the dynamical magnetoelectric coupling [6]. In Ni_2CoTeO_6 and $NiCo_2TeO_6$, where the Co^{2+} randomly substitutes Ni^{2+} across all three symmetry inequivalent Ni sites, long-range magnetic order develops below 55 and 52 K, respectively, consisting of ferromagnetically coupled a-b layers of Ni^{2+} that rotate along c with an incommensurate propagation vector $\mathbf{k} = (0\ 0\ \frac{3}{2} \pm \delta)$, where $\delta = 0.201$ and 0.289, respectively [6]. Similar to Ni_3TeO_6, an anomaly was observed in the dielectric susceptibility at T_N for both samples, suggesting the presence of magnetoelectric behavior, and at least one electromagnon [6].

In this study we investigate the structural and magnetic chiralities in $NiCo_2TeO_6$ by combining polarized x-ray and neutron diffraction on single-crystal samples. We have successfully applied this method to identify both chiralities in two enantiopure Langasite $Ba_3NbFe_3Si_2O_{14}$ samples of different structural handedness [11] and it could be shown that the crystal and magnetic chiralities are coupled through the magnetic anisotropy energy. While in the Langasite compound a uniform crystal chirality is established, which can be charaterized by the twist of the Fe-O-O-Fe superexchange pathways, $NiCo_2TeO_6$ is a ferri-chiral system, i.e., two intertwined helices with opposite handednesses and different *degrees* of structural chirality create a net chirality. The degree of structural chirality can be quantified using the continuous chirality measure (CCM, see [12]), defined as the minimal normalized squared atomic displacement required to transform the structure into its closest achiral configuration. The CCM is a dimensionless quantity normalized to the interval [0,1], where CCM = 0 corresponds to a perfectly achiral structure and CCM = 1 to a maximally chiral one. Figure 1(a) shows the crystal structure of $NiCo_2TeO_6$ emphasizing the

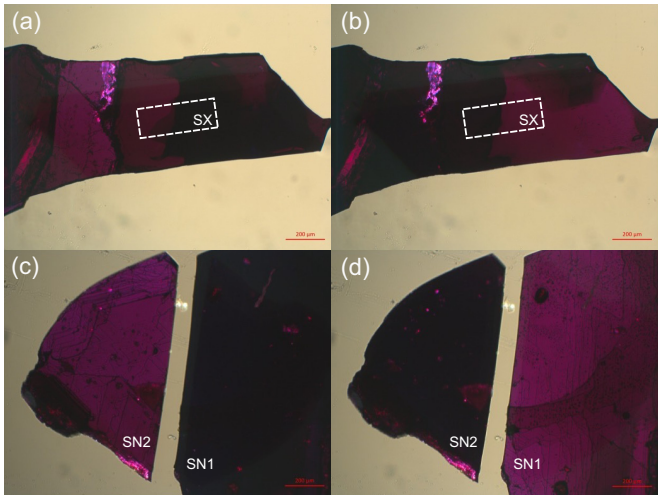

FIG. 2. Transmission polarized optical microscope images showing the single-crystal samples used in this study. The pictures were taken along the optically active c axis of the Nickelate samples. (a) and (b) show the heterochiral sample SX with the dashed rectangle indicating the surface probed in the polarized x-ray experiments, while (c) and (d) show the two samples used in the polarized neutron experiments—SN1 and SN2—revealing a largely homochiral volume for SN2 and some islands as well as a shaded region of different contrast for SN1 suggesting a minor volume fraction of opposite chirality. The images (b) and (d) are taken with a different polarizer/analyzer angle with respect to (a) and (c) and reveal a different contrast for the structural twins.

network of edge- and facesharing MO_6 and TeO_6 octahedra, while Figs. 1(b) and 1(c) reveal the opposite chiralities of the O1 and O2 screws propagating along the c axis. Due to a different CCM resulting from different distortions of the triangular motifs [see Fig. 1(d)], the opposite rotations do not cancel each other and the structure is characterized by a net chirality. Our results clearly show that—despite of the ferri-chiral nature of the crystal structure—a single magnetic chirality is established which is intimately coupled to the net chirality of the crystal lattice.

II. EXPERIMENTAL

The same conventions as detailed in [11] were used both for the x-rays and the neutron experiments.

A. X-ray scattering

Resonant elastic x-ray scattering (REXS) measurements were performed on the I16 beamline [13] at the Diamond Light Source on a polished sample of $NiCo_2TeO_6$ of 0.05 mm thickness from which a surface of 0.15 by 0.4 mm was measured [sample SX, see Figs. 2(a) and 2(b)]. Ni, Co and Te all have resonant edges accessible at the I16 beamline. To simultaneously measure both the magnetic and structural chirality, the beamline could either be aligned at the Ni K edge or Co K edge, as only Ni and Co are expected to develop long-range magnetic order. The ratio of Ni to Co ions in the sample is 1:2, therefore the x-ray scattering at the Co edge is expected to be larger than that at the Ni K edge.

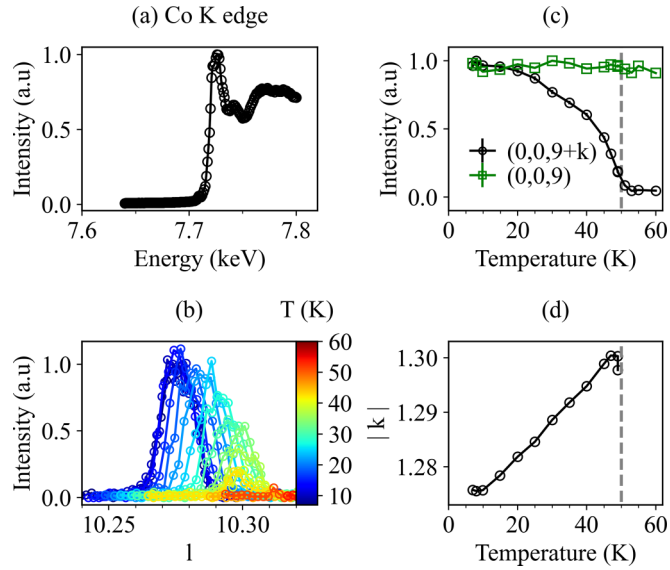

FIG. 3. (a) An x-ray absorption spectrum taken about the Co K edge. (b) Line scans taken in the l direction showing the magnetic satellite of the (0 0 9) reflection with propagation vector $\mathbf{q} = (0\ 0\ 1.29)$, taken as the sample was warmed between 7 and 60 K. The temperature dependence of (c) the integrated intensity of both the (0 0 9) charge reflection and the $(0\ 0\ 9 + \mathbf{q})$ magnetic satellite and (d) the magnitude of the magnetic propagation vector. The dashed lines denote the onset of magnetic ordering at $T_N = 50$ K.

Furthermore, the enhancement to the magnetic scattering is larger at the Co K edge owing to Co having a larger orbital angular momentum. Therefore, we aligned the beamline at 7.709 keV, the Co K edge. An x-ray absorption spectrum taken about the Co K edge is shown in Fig. 3(a) and demonstrates a large enhancement to the fluorescence intensity as the energy of the incident beam was tuned through the edge. Measurements were performed in the vertical scattering geometry with an incident beam size of 180 μm in the horizontal direction and 30 μm in the vertical. The sample was mounted onto a copper sample holder using silver paste such that the $[0\,0\,l]$ direction was specular. The azimuthal reference was $[h\,0\,0]$, such that at $\psi = 0$ the a axis was parallel to the incident beam. A closed cycle refrigerator (Advanced Research Systems) was used to cool the sample from room temperature to 5 K. A Pilatus 100 K area detector was used to measure the diffracted intensity. At 7.709 keV the attenuation length of the x-rays is expected to be approximately 10 μm for an incident angle greater than 40°, which serves as an estimate for the x-ray penetration depth. The incident polarization of light was tuned between linear horizontal (σ), linear vertical (π) and two circular polarizations of light, left circular ↺ and right circular ↻.

B. Neutron scattering

Polarized neutron diffraction experiments were carried out on the spin-polarized hot-neutron beam facility D3 at the Institut Laue-Langevin (Grenoble, France). A polarized neutron beam ($\lambda = 0.83$ Å, $p_0 = 0.93$) is obtained from the (1 1 1) reflection of a Cu_2MnAl Heusler monochromator that is placed within a permanent magnetic field. Two thin as-grown

crystals (thickness less than 50 μm) of approximate masses 0.3 and 0.9 mg, respectively, identified to be largely homochiral and to reveal opposite net structural chiralities using optical microscope techniques [samples SN1 and SN2, see Figs. 2(c) and 2(d)], were placed inside the zero-field chamber of the Cryogenic Polarization Analysis Device (Cryopad [14,15]) with the crystallographic b axis parallel to the vertical axis of the diffractometer giving access to the (h 0 l) scattering plane. The structural chirality was investigated by probing the interference between nuclear and spin-orbit (Schwinger [16]) scattering amplitudes in Bragg condition. By reversing the polarization of the incoming neutron beam flipping ratios have been measured without the need of polarization analysis. The magnetic chirality was determined using spherical neutron polarimetry (SNP) by keeping the incoming polarization fixed and by analyzing the polarization of the beam scattered from purely magnetic Bragg reflections with the help of a ^{3}He neutron spin filter which is hosted by Decpol, a compact detector shielding providing the homogeneous holding-field required for the long relaxation time (half-life of typically 100 hours) of the ^{3}He polarization. The analyzing efficiency p_f of the ^{3}He spin filter cell was periodically monitored by measuring the beam polarization after scattering from a purely nuclear peak and all presented data were corrected for the time-dependent decay. According to the local reference for each Bragg reflection, where **x** is parallel to the scattering vector **Q**, **z** is parallel to the vertical direction and **y** completes the orthogonal right-handed set, full polarization matrices were collected on different magnetic Bragg peaks by aligning the incident and analyzing the final polarization vector along these three directions, respectively. The chiral terms, which can be accessed by analyzing the polarization created along **x** for an incident neutron beam polarized along **y** or **z**, contain direct information about the handedness of the magnetic helix. All neutron data were analyzed using MAG2POL [17].

III. RESULTS AND DISCUSSION

A. X-ray scattering

Magnetic satellites with propagation vector $\mathbf{q} = (0\ 0\ 1.297(5))$ were observed to appear below $T_N = 50$ K, in close agreement with the reported magnetic propagation vector and transition temperature of $Ni_{3-x}Co_xTeO_6$ [6]. The intensity and propagation vector of the magnetic satellite about the (0 0 9) reflection was measured as the sample was warmed from 7 K to above T_N Fig. 3(b). The intensity of the magnetic satellite gradually decreased, with a dependence consistent with that of a second-order phase transition as shown in Fig. 3(c), while the magnitude of the propagation vector increased linearly as the sample was warmed Fig. 3(d).

1. Magnetic chiral domains

The intensity of x-rays scattered from a noncollinear magnetic structure will differ for a given reflection when probed with incident ↺ polarized light and incident ↻ polarized light. Therefore, a contrast in scattered magnetic intensity when measured with the two circular polarizations of light is indicative of a noncollinear magnetic structure. Furthermore, the ratio of scattered intensity using incident ↺ and ↻ polarized light flips sign when measuring magnetic chiral domains of opposite handedness. Therefore, circular polarized light may also be used to probe magnetic domains. The magnetic satellite of the (0 0 9) reflection (+**q**) was measured, first with incident ↺ polarized light, followed by incident ↻ polarized light. As $NiCo_2TeO_6$ was determined to have a noncollinear helical magnetic structure [6], one should observe a difference in the scattered magnetic intensity when using the two circular polarizations of light, and if magnetic chiral domains are present the difference should flip sign when probing a magnetic domain of opposed handedness. First the size of the beam was focused to 40 by 30 μm, and then the beam was translated across the sample as the magnetic (0 0 9)+**q** reflection was measured with both circular polarizations of light. A contrast in the scattered magnetic intensity was observed, which flipped in sign when probing two different parts of the sample SX, labeled P_1 and P_2, as shown in Figs. 4(a) and 4(b). Of the portion of the sample probed, two magnetic chiral domains were measured, wherein each magnetic chiral domain spanned an area of at least 0.1 mm^2.

2. Structural chiral domains

To probe the structural chirality we followed the methodology as outlined in [11], which relies on the sensitivity of a linearly polarized x-ray beam to the structural chirality of the sample owing to the interference from the anomalous part of the atomic form factor. First we simulated the x-ray energy dispersion of both structural chiral enantiomers for several reflections to identify a reflection that would provide a significant contrast in intensity upon measurement of the two enantiomers. These simulations are given in Fig. S1 of the Supplemental Material [18]. Once a suitable reflection was identified, the (0 1 11) reflection in this instance, the beam was centered at positions P_1 and P_2 of sample SX and the x-ray energy dispersion of the (0 1 11) reflection was measured. We found that the x-ray energy dispersion showed markedly different behavior; the slope of the dispersion had an upward trajectory after the Co K edge for position P_1 and a downward trajectory after the Co K edge for position P_2, in agreement with the simulation of the (0 1 11) reflection for the two structural enantiomers of $NiCo_2TeO_6$. These measurements demonstrated two things: firstly that the structure of $NiCo_2TeO_6$ is chiral, and secondly that the measured sample is not enantiopure. To image the variation of the structural chiral domains across the sample we measured the (0 1 11) reflection, first at 7.6 and then again at 7.8 keV. The sign of the normalized ratio of the integrated intensity of the reflection measured at 7.6 and 7.8 keV will be opposite for the chiral enantiomers, and hence this measurement is a direct probe for the structural chiral domains in the sample. Figure 4(f) shows that the portion of the measured sample clearly had two structural chiral domains, as observed for the magnetic chiral domains. However in comparison to the boundary between the magnetic chiral domains, which was relatively sharp, the boundary between the structural domains seems broader and less well defined. This could be an artefact originating from locally varying surface quality of the sample and insufficient accuracy of the measured x-ray data especially in those regions. Overall the measurements demonstrate a clear

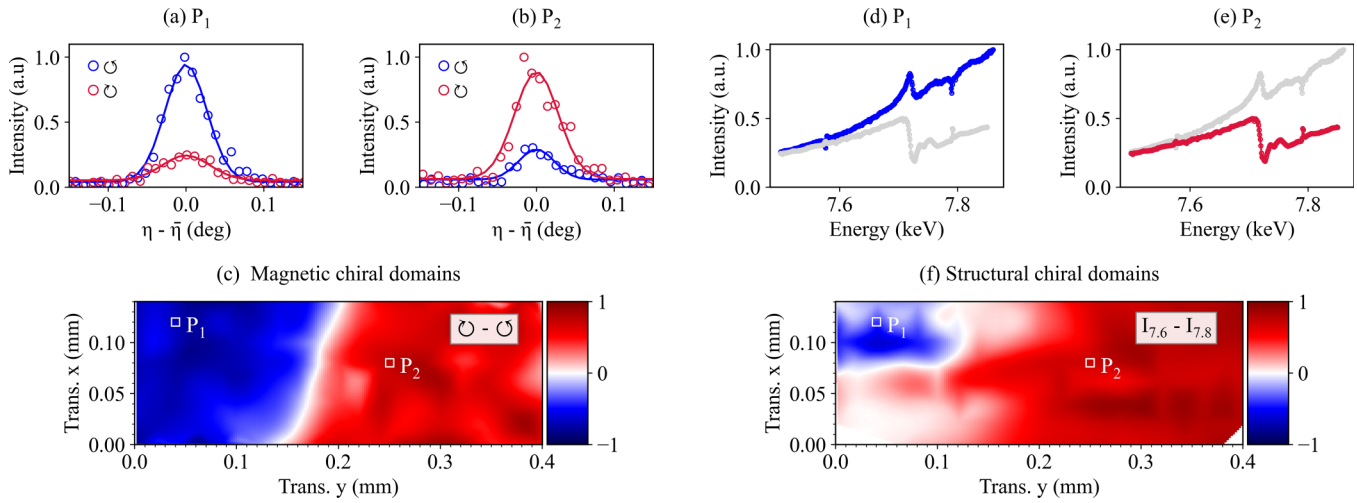

FIG. 4. Rocking curve scans taken at 7 K about the magnetic satellite of the (0 0 9) reflection with propagation vector **q** measured with both circular polarizations of light and shown at sample positions (a) P_1 and at (b) P_2. (c) A raster of the sample showing the magnetic chiral domains taken by translating the 40 x 30 μm beam across the sample and measuring $\frac{I_{\circlearrowleft}-I_{\circlearrowright}}{I_{\circlearrowleft}+I_{\circlearrowright}}$ (the difference in the integrated intensity of the two circular polarizations of light, normalized by the sum of the integrated intensity) of the magnetic satellite of the (0 0 9) with propagation vector **q** (a cubic interpolation method was used to create the final maps). X-ray energy dispersion of the (0 1 11) reflection taken with incident σ-polarized light at positions (d) P_1 (blue symbols) and at (e) P_2 (red symbols). For direct comparison, the data corresponding to the opposite chirality are additionally shown as gray symbols. (f) A raster of the sample showing the structural chiral domains taken by translating the beam across the sample and measuring $\frac{I_{7.6}-I_{7.8}}{I_{7.6}+I_{7.8}}$ (the difference in the integrated intensity of the (0 1 11) reflection measured at 7.6 and at 7.8 keV, normalized by the sum of their integrated intensity). The positions P_1 and P_2 with respect to the rest of the sample are shown by the solid white square markers in (c) and (f).

coupling between the magnetic and structural chiral domains in $NiCo_2TeO_6$, but which is not true at the domain boundary and therefore may indicate different physics in this region.

B. Neutron diffraction

1. *Structural chirality*

Adequate reflections for the experimental detection of Schwinger scattering were identified using MAG2POL [17] by generating a list of Bragg reflections with the largest flipping ratio asymmetry $R-1$ based on the structural details given in the Supplemental Material of [6] (data recorded at 3 K on the high-resolution powder diffractometer D2B, ILL, Grenoble). Given the small sample volume and consequently weak scattered intensities we concentrated on those Bragg reflections with the strongest nuclear structure factors V_N, which amplify the spin-orbit scattering amplitude V_{SO} through the interference term $\mathcal{I}$ in

$$R = \frac{V_N^2 + V_{SO}^2 + \mathcal{I}}{V_N^2 + V_{SO}^2 - \mathcal{I}}$$

with

$$\mathcal{I} = p(V_N \cdot V_{SO}^* + V_N^* \cdot V_{SO}) = 2p\mathrm{Re}(V_N \cdot V_{SO}^*)$$

and

$$V_{SO}(\mathbf{Q}) = i\frac{\gamma r_0}{2} \cdot \frac{m_e}{m_p} \cdot F_E(\mathbf{Q}) \cot(\theta) \cdot \hat{\boldsymbol{\sigma}} \cdot \mathbf{z},$$

where $\gamma = -1.913$ is the neutron gyromagnetic ratio in units of the nuclear magneton μ_N, r_0 is the classical electron radius, m_e and m_p are the electron and proton masses, $\hat{\boldsymbol{\sigma}}$ is the neutron spin operator and $F_E(\mathbf{Q})$ is the electrostatic unit cell structure factor given by

$$F_E(\mathbf{Q}) = -\sum_j [Z_j - f_j(\mathbf{Q})] T_j \exp(-i\mathbf{Q}\mathbf{r}_j)),$$

where Z_j is the atomic number of site j and $f_j(\mathbf{Q})$ the x-ray atomic form factor for this ion. As described in Sec. II the incident neutron beam polarization $\hat{\boldsymbol{\sigma}}$ is either parallel or antiparallel to the vertical direction **z**. Figure 5 shows the observed flipping ratios of the bigger sample, denoted

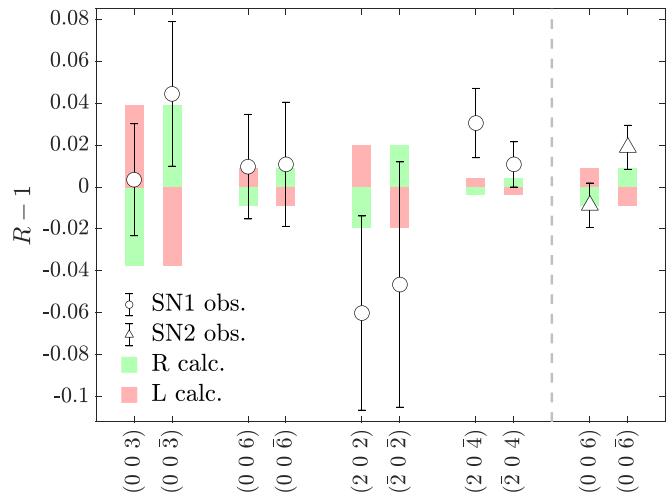

FIG. 5. Observed asymmetry of flipping ratios ($R-1$) for sample SN1 (circles) and sample SN2 (triangles) shown together with the calculated values for a right-handed (R, green bars) and left-handed (L, red bars) net chirality.

as SN1, for four different Friedel pairs (to the left of the dashed line), together with the theoretically expected values for an enantiopure sample of either handedness. It has to be noted that the flipping ratio asymmetry is inverted between a left-handed and a right-handed sample and also between the two reflections of a Friedel pairs. As can be seen, the results for sample SN1 are inconclusive, because of the overlapping error bars between two reflections of a Friedel pair (for a measuring time of 90 minutes per flipping ratio), for which no significant inverted asymmetry can be deduced. A possible explanation is the presence of both inversion twins in the used sample which is supported by the investigation of the magnetic chiralities as will be shown in Sec. III B 2. The smaller sample, labeled SN2, showed significantly weaker scattered intensities, for which we concentrated on producing conclusive data on only one Friedel pair. Flipping ratios of the (0 0 6) and (0 0 $\bar{6}$) reflections were measured for 22 and 36 hours, respectively, revealing significant and inverted asymmetries $R-1$ as shown in Fig. 5 to the right of the dashed line. The result indicates chiral homogeneity of the sample and seems to be in agreement with the calculated values for a right-handed structure. However, this still does not permit an unambiguous determination of the absolute structural chirality, which is due to a nonunique indexation of (h k l) reflections. In the present case, flipping ratios different from unity are absent in the (h k 0) plane and can be found in the (h 0 l) plane, which was employed in this experiment. Even by taking into account the general extinction rules of space group $R3$ and the intensity relations between different observable reflections (also considering reflections above and below the scattering plane), there always exist two possibilities to index the observed reflections. And these two possibilities, e.g., an observed (0 0 6) reflection can also be labeled as (0 0 $\bar{6}$), reverse the flipping ratios and therefore make it impossible to unambiguously determine the absolute structural chirality. Note that in the case of the Langasite study [11], Schwinger scattering is observed in the (h k 0) plane and likewise different indexation options are possible. However, these options are indifferent with respect to the flipping ratios, e.g., a (2 2 0) could be labeled as ($\bar{4}$ 2 0), but $R_{(220)} = R_{(\bar{4}20)}$, because they are related by the threefold rotation axis, which therefore allows a unique attribution to a left- or right-handed chirality. Due to the ambiguity with (h 0 l) reflections in the $R3$ case we have reinvestigated the same single crystal on I16, which confirmed its enantiopurity and a right-handed net chirality. (Fig. S2 of the Supplemental Material [18]).

2. *Magnetic chirality*

The Blume-Maleev equations [19,20], which relate the initial (i) and final (f) neutron spin with generalized cross sections, can be written in matrix form yielding what is generally called the *polarization matrix* of a Bragg reflection with elements P_{fi}. The magnetic chirality of sample SN1 was probed by analyzing several full polarization matrices obtained by the SNP method. In the present case, the measured Bragg peaks are of purely magnetic nature, for which nuclear and nuclear-magnetic interference terms can be omitted resulting in a simplified polarization matrix given by

$$\mathbf{P} = \begin{pmatrix} \frac{-p_0 M_\perp^2 - J_{yz}}{I_x} & \frac{-J_{yz}}{I_y} & \frac{-J_{yz}}{I_z} \\ 0 & \frac{p_0(M_{\perp y}^2 - M_{\perp z}^2)}{I_y} & 0 \\ 0 & 0 & \frac{p_0(-M_{\perp y}^2 + M_{\perp z}^2)}{I_z} \end{pmatrix},$$

with $M_{\perp y}^2 = M_{\perp y} M_{\perp y}^*$, $M_{\perp z}^2 = M_{\perp z} M_{\perp z}^*$, and $M_\perp^2 = \mathbf{M}_\perp \mathbf{M}_\perp^*$ (with $\mathbf{M}_\perp$ being the magnetic interaction vector). The scattered intensities are $I_x = M_\perp^2 + p_{ix} J_{yz}$ and $I_y = I_z = M_\perp^2$ for an incident neutron beam polarized along the x and along the y or z axes, respectively. The decisive term in this study is $J_{yz} = 2\,\mathrm{Im}(M_{\perp y} M_{\perp z}^*)$, the so-called chiral term, whose sign is a direct measure of the handedness of the magnetic spiral along the propagation vector. Note that $J_{yz} = P_{xy} = P_{xz} = 0$ means either a nonchiral magnetic structure or two chiral magnetic domains with inverted handedness and equal domain population. The latter implies that for a known chiral magnetic structure the population of the eventual inversion domains can be extracted from the SNP data, which is inaccessible with unpolarized neutrons. The magnetic structure is described by the magnetic superspace group $R3.1(0, 0, \gamma)ts$ and the magnetic moment values have been adopted from [6]. The observed and calculated polarization matrices of different (0 0 l) $\pm$ **q** reflections are shown in Fig. 6. Note that for a circular helix with Fourier components in the a-b plane and magnetic Bragg reflections with $\mathbf{x} \parallel \mathbf{Q} \parallel \mathbf{c}$ (therefore $M_{\perp y} = iM_{\perp z}$) the chiral term J_{yz} contains the full projection of $M_{\perp y}$ and $M_{\perp z}$, therefore the elements P_{xy} and P_{xz} should be $+1$ or -1 for a single magnetic domain depending on its handedness, since $J_{yz} = 2\,\mathrm{Im}(M_{\perp y} M_{\perp z}^*) = M_{\perp y}^2 + M_{\perp z}^2 = M_\perp^2$. With values between 0.30 and 0.58 throughout all measured reflections the moduli of the polarization matrix terms P_{xy} and P_{xz} are significantly smaller than 1, which is in agreement with a mixture of two inversion twins. The fact that the P_{xy} and P_{xz} terms change their sign upon inverting the polarization and analysis axes for the same reflection (labeled as σ^{--} in Fig. 6(a)) is a direct proof of a chiral magnetic structure. In a global refinement to six full polarization matrices where only the population of two inversion twins—assuming a single magnetic helix chirality within each of these twins—were refined, we find a significantly heterochiral distribution of 0.738(6):0.262(6) with a majority left-handed helix. Based on this result, the maximal asymmetry in the Schwinger scattering flipping ratios $R-1$ would be 0.018 for the (0 0 6) reflection (in comparison to 0.039 for an enantiopure sample, cf. Fig. 5). The agreement of the published magnetic structure with the observed polarimetry data is very good ($\chi^2 = 3.4$) as can be seen in Fig. 6. The fact that $P_{yy} \approx 0$ and $P_{zz} \approx 0$ is in agreement with a circular envelope of the helical modulation, which yields $M_{\perp y}^2 = M_{\perp z}^2$. Although the magnetic superspace group $R3.1(0, 0, \gamma)ts$ imposes basis vectors producing a circular envelope we have verified an eventual ellipticity which can be confirmed to be insignificant. It is important to note at this point that the presence of two inversion twins is not the unique explanation of the SNP data. The presence of three symmetry independent Ni/Co sites would in principle allow to define helices with

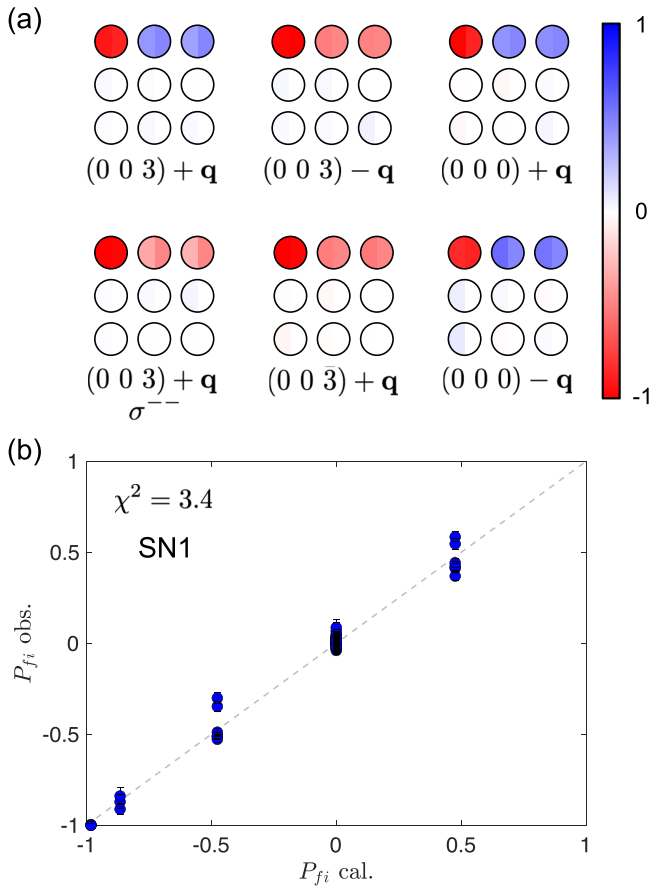

FIG. 6. (a) Full polarization matrices of the purely magnetic (0 0 l)±**q** reflections recorded using sample SN1. For each element the left (right) half of the circle represents the observed (calculated) value according to the color bar to the right. For the (0 0 3)+**q** σ^{--} reflection the polarization and analysis axes were inverted with respect to the other measurements. (b) All polarization matrix elements from (a) in an observed versus calculated plot with the dashed line meaning P_{fi} obs. = P_{fi} cal.

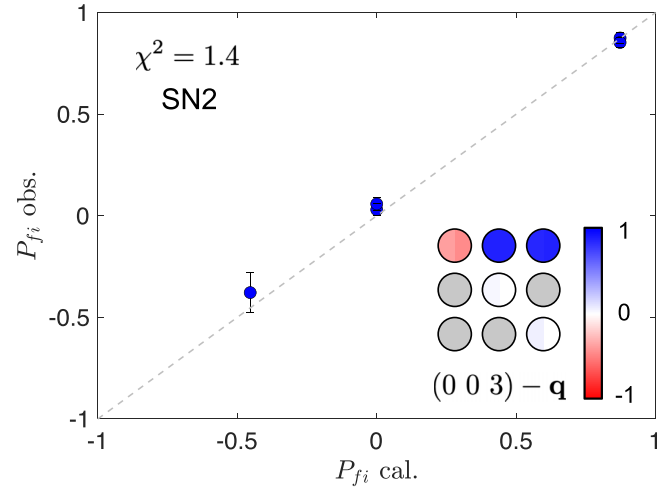

FIG. 7. Polarization matrix elements of the purely magnetic (0 0 3)-**q** reflection—recorded using sample SN2—in an observed-vs-calculated plot together with a straight (dashed) line indicating the excellent agreement. The inset to the lower right shows the polarization matrix in a color-coded plot. For each element the left (right) half of the circle represents the observed (calculated) value, whereas elements that were not measured are shown in gray.

mutually opposite handedness within a structurally enantiopure crystal. On the other hand, a symmetry reduction from *R*3 to *P*3 would allow to have different columns of Ni/Co spins (formerly related by the *R*-centering translations) with opposite rotations along the *c* axis. All these scenarios cannot be distinguished based on the SNP data presented beforehand, but a decisive clue—unambiguously pointing towards one of these scenarios—was obtained by investigating sample SN2 as will be shown here below. For the much smaller sample SN2 only the diagonal and chiral elements of the polarization matrix on the (0 0 3)-**q** reflection could be investigated on a reasonable time scale which are shown in Fig. 7. Nevertheless, a clear indication of a nearly homochiral sample is present on the P_{xy} and P_{xz} elements amounting to 0.87(3) and 0.85(3), respectively. A similar fit as for sample SN1, i.e., by only refining the population of two inversion twins, reveals a distribution of 0.064(9):0.936(9) with a close to enantiopure right-handed helix. This result also definitely discards the possibility of counter-propagating helices either along different Ni/Co columns or among the three distinct Ni/Co sites.

IV. CONCLUSIONS

Our combined polarized x-ray and neutron scattering study establishes a clear relationship between the structural and magnetic chiralities in the magnetoelectric compound $NiCo_2TeO_6$. Micrometer-resolution REXS raster images using linear and circular polarizations of light demonstrate an unambiguous direct coupling between the net handedness of the ferri-chiral nuclear structure and the handedness of the magnetic helix within a single chiral domain of at least 0.1 mm^2. The simultaneous switching of both chiralities could be observed by translating the microfocused beam on a heterochiral sample over a studied surface of 0.4 x 0.15 mm^2. While the domain boundary between the magnetic chiral domains is sharp, around a few tens of microns in size, the boundary region between the structural chiral domains seems more extended which may be caused by locally varying sample surface quality and the accuracy of the measured x-ray intensities. Although the interlocking between chiral and polar domain walls was established [4] and leads to a low domain wall energy due to the preservation of the ideal octehdra stacking, an eventually more complex picture concerning the net chirality resulting from the two opposite O1 and O2 helices cannot be ruled out based on our results. Our polarized neutron data are not conclusive concerning the structural chirality because of the very weak spin-orbit (Schwinger) scattering—apparent through the m_e/m_p prefactor in the spin-orbit scattering amplitude—and the limitation in the available sample volume. Polarized neutron experiments inherently suffer from a significant flux and counting-rate penalty, for which the experimental determination of Schwinger flipping ratios with small samples is extremly challenging, hence the rather large error bars shown in Fig. 5. Futhermore, it is impossible to deduce the absolute structural chirality due to the relation

between the available scattering plane for nonzero spin-orbit scattering cross sections and the symmetry elements of the crystal structure. On the other hand, our SNP experiments yield clear quantitative results and unambiguously reveal that 94% of the bulk single-crystal sample hosts a right-handed magnetic spiral. This suggests a homochiral magnetic helicity in the presence of two intertwined structural helices formed by O1 and O2 ions with a net chirality of the same handedness as the magnetic one. The microscopic origin, based on the balance of exchange and possible Dzyaloshinskii-Moriya interactions as well as eventual magnetostriction effects, is still unknown and beyond the scope of this work. In summary, our work on $NiCo_2TeO_6$, a system with interesting magnetoelectric properties and enhanced dynamic magnetoelectric coupling with potential for the realization of future magnetoelectric devices, adds valuable information concerning the coupling between the magnetic and structural chiralities. Our results provide the basis for eventual theoretical approaches allowing to better understand the microscopic origin and therefore the exploitation of the magnetoelectric properties.

ACKNOWLEDGMENTS

We acknowledge Diamond Light Source for time on Beamline I16 under Proposals No. MM30525-1, No. MM32584-1, No. MM33189-1, and No. CM31138-23. We acknowledge the Institut Laue-Langevin for the beam time on the polarized hot-neutrons diffractometer D3 [21]. Work at POSTECH was supported by the National Research Foundation of Korea (NRF) funded by the Ministry of Science and ICT (Grant No. RS-2022-NR068223). The work at Rutgers University was supported by the DOE under Grant No. DOE: DE-FG02-07ER46382.

DATA AVAILABILITY

Some of the data that support the findings of this article are openly available [21], embargo periods may apply. Polarized x-ray data are not publicly available upon publication because it is not technically feasible and/or the cost of preparing, depositing, and hosting the data would be prohibitive within the terms of this research project. The data are available from the authors upon reasonable request.

[1] R. Wakatsuki, Y. Saito, S. Hoshino, Y. M. Itahashi, T. Ideue, M. Ezawa, Y. Iwasa, and N. Nagaosa, Nonreciprocal charge transport in noncentrosymmetric superconductors, Sci. Adv. **3**, e1602390 (2017).

[2] S. Mülbauer, B. Binz, F. Jonietz, C. Pfleiderer, A. Rosch, A. Neubauer, R. Georgii, and P. Böni, Skyrmion lattice in a chiral magnet, Science **323**, 915 (2009).

[3] A. N. Bogdanov and C. Panagopoulos, Physical foundations and basic properties of magnetic skyrmions, Nat. Rev. Phys. **2**, 492 (2020).

[4] X. Wang, F.-T. Huang, J. Yang, Y. S. Oh, and S.-W. Cheong, Interlocked chiral/polar domain walls and large optical rotation in Ni_3TeO_6, APL Mater. **3**, 076105 (2015).

[5] A. M. Sargent, K. A. Smith, X. Xu, K. Du, S.-W. Cheong, L. Wehmeier, G. L. Carr, and J. L. Musfeldt, Near-field infrared imaging of polar domain walls in Ni_3TeO_6, J. Appl. Phys. **138**, 055302 (2025).

[6] S. Skiadopoulou, M. Retuerto, F. Borodavka, C. Kadlec, F. Kadlec, M. Míšek, J. Prokleška, Z. Deng, X. Tan, C. Frank, J. A. Alonso, M. T. Fernández-Díaz, M. Croft, F. Orlandi, P. Manuel, E. McCabe, D. Legut, M. Greenblatt, and S. Kamba, Structural, magnetic, and spin dynamical properties of the polar antiferromagnets $Ni_{3-x}Co_xTeO_6$ ($x = 1, 2$), Phys. Rev. B **101**, 014429 (2020).

[7] I. Živković, K. Prša, O. Zaharko, and H. Berger, Ni_3TeO_6–a collinear antiferromagnet with ferromagnetic honeycomb planes, J. Phys.: Condens. Matter **22**, 056002 (2010).

[8] Y. S. Oh, S. Artyukhin, J. J. Yang, V. Zapf, J. W. Kim, D. Vanderbilt, and S.-W. Cheong, Non-hysteretic colossal magnetoelectricity in a collinear antiferromagnet, Nat. Commun. **5**, 3201 (2014).

[9] S. Skiadopoulou, F. Borodavka, C. Kadlec, F. Kadlec, M. Retuerto, Z. Deng, M. Greenblatt, and S. Kamba, Magnetoelectric excitations in multiferroic Ni_3TeO_6, Phys. Rev. B **95**, 184435 (2017).

[10] J. Lass, C. R. Andersen, H. K. Leerberg, S. Birkemose, S. Toth, U. Stuhr, M. Bartkowiak, C. Niedermayer, Z. Lu, R. Toft-Petersen, M. Retuerto, J. O. Birk, and K. Lefmann, Field-induced magnetic incommensurability in multiferroic Ni_3TeO_6, Phys. Rev. B **101**, 054415 (2020).

[11] N. Qureshi, A. Bombardi, S. Picozzi, P. Barone, E. Lelièvre-Berna, X. Xu, C. Stock, D. F. McMorrow, A. Hearmon, F. Fabrizi, P. G. Radaelli, S.-W. Cheong, and L. C. Chapon, Absolute crystal and magnetic chiralities in the langasite compound $Ba_3NbFe_3Si_2O_{14}$ determined by polarized neutron and x-ray scattering, Phys. Rev. B **102**, 054417 (2020).

[12] H. Zabrodsky and D. Avnir, Continuous symmetry measures. 4. Chirality, J. Am. Chem. Soc. **117**, 462 (1995).

[13] S. P. Collins, A. Bombardi, A. R. Marshall, J. H. Williams, G. Barlow, A. G. Day, M. R. Pearson, R. J. Woolliscroft, R. D. Walton, G. Beutier, and G. Nisbet, Diamond beamline I16 (materials & magnetism), AIP Conf. Proc. **1234**, 303 (2010).

[14] F. Tasset, P. J. Brown, E. Lelièvre-Berna, T. Roberts, S. Pujol, J. Allibon, and E. Bourgeat-Lami, Spherical neutron polarimetry with Cryopad-II, Physica B **267**, 69 (1999).

[15] E. Lelièvre-Berna, E. Bourgeat-Lami, P. Fouilloux, B. Geffray, Y. Gibert, K. Kakurai, N. Kernavanois, B. Longuet, F. Mantegezza, M. Nakamura, S. Pujol, L.-P. Regnault, F. Tasset, M. Takeda, M. Thomas, and X. Tonon, Advances in spherical neutron polarimetry with cryopad, Physica B **356**, 131 (2005).

[16] J. Schwinger, On the polarization of fast neutrons, Phys. Rev. **73**, 407 (1948).

[17] N. Qureshi, Mag2Pol: A program for the analysis of spherical neutron polarimetry, flipping ratio and integrated intensity data, J. Appl. Cryst. **52**, 175 (2019).

[18] See Supplemental Material at http://link.aps.org/supplemental/10.1103/mxdc-pl82 for the x-ray energy dispersion simulations and structural chirality of sample SN2.

[19] M. Blume, Polarization effects in the magnetic elastic scattering of slow neutrons, Phys. Rev. **130**, 1670 (1963).

[20] S. V. Maleev, V. G. Bar'yaktar, and P. A. Suris, The scattering of slow neutrons by complex magnetic structures, Sov. Phys. Solid State **4**, 2533 (1963).

[21] N. Qureshi, K. Beauvois, A. Bombardi, L. Chapon, S.-W. Cheong, J. A. Rodríguez-Velamazán, A. Stunault, and A. M. Vibhakar, Interplay between structural and magnetic chiralities in $Ni_{3-x}Co_xTeO_6$ (2024), https://doi.ill.fr/10.5291/ILL-DATA.DIR-315.